

Simultaneous achievement of large anomalous Nernst effect and reduced thermal conductivity in sintered polycrystalline topological Heusler ferromagnets

Koichi Oyanagi, Hossein Sepehri-Amin*, Kenta Takamori, Terumasa Tadano, Takumi Imamura, Ren Nagasawa, Krishnan Mahalingam, Takamasa Hirai, Fuyuki Ando, Yuya Sakuraba, Satoru Kobayashi, and Ken-ichi Uchida**

K. Oyanagi, K. Takamori, T. Imamura, S. Kobayashi

Faculty of Science and Engineering, Iwate University, Morioka 020-8551, Japan

E-mail: k.oyanagi444@gmail.com

K. Oyanagi, H. Sepehri-Amin, T. Tadano, T. Imamura, R. Nagasawa, K. Mahalingam, T. Hirai, F. Ando, Y. Sakuraba, K. Uchida

Research Center for Magnetic and Spintronic Materials, National Institute for Materials Science (NIMS), Tsukuba 305-0047, Japan

E-mail: H.SEPEHRIAMIN@nims.go.jp, UCHIDA.Kenichi@nims.go.jp

K. Oyanagi

Center for Sustainable Materials and Interfacial Science, Iwate University, Morioka 020-8551, Japan

T. Imamura, R. Nagasawa, Y. Sakuraba, K. Uchida

Graduate School of Science and Technology, University of Tsukuba, Tsukuba 305-8573, Japan

K. Uchida

Department of Advanced Materials Science, Graduate School of Frontier Sciences, The University of Tokyo, Kashiwa 277-8561, Japan

Keywords: anomalous Nernst effect, microstructure characterization, magnetic topological materials, phonon first principal calculation, transverse thermoelectric conversion

This study reports the observation of the large anomalous Nernst effect in polycrystalline ferromagnetic Co₂MnGa (CMG) slabs prepared by a spark plasma sintering method. By optimizing the sintering conditions, the anomalous Nernst coefficient reaches $\sim 7.5 \mu\text{V K}^{-1}$ at room temperature, comparable to the highest value reported in the single-crystalline CMG slabs. Owing to the sizable anomalous Nernst coefficient and reduced thermal conductivity, the dimensionless figure of merit in our optimized CMG slab shows the record-high value of $\sim 8 \times 10^{-4}$ at room temperature. With the aid of the nano/microstructure characterization and first-principles phonon calculation, this study discusses the dependence of the transport properties on the degree of crystalline ordering and morphology of crystal-domain boundaries in the sintered CMG slabs. The results reveal a potential of polycrystalline topological materials for transverse thermoelectric applications, enabling the construction of large-scale modules.

1. Introduction

The anomalous Nernst effect (ANE) refers to the conversion of a longitudinal heat current into a transverse electric field in a magnetic material with spontaneous magnetization. Because of the transverse geometry of the thermoelectric conversion, ANE enables the construction of thermoelectric devices with convenient scalability and easy fabrication.^[1-4] The output voltage of ANE increases simply by increasing a length of the device perpendicular to the applied temperature gradient, realizing a large-scale and junction-less thermoelectric module, which cannot be achieved by the Seebeck effect used in conventional thermoelectric modules. However, low thermoelectric conversion performance of ANE prohibits practical applications for thermoelectric devices.

The thermoelectric conversion performance of ANE is often evaluated by the dimensionless figure of merit:^[5-7]

$$z_{\text{ANE}}T = \frac{S_{\text{ANE}}^2 \sigma}{\kappa} T, \quad (1)$$

where S_{ANE} is the anomalous Nernst coefficient, σ the electric conductivity, and κ the thermal conductivity at absolute temperature T . Up to now, a major strategy for improving $z_{\text{ANE}}T$ is finding materials showing large S_{ANE} . In this context, topological magnets exhibiting large ANE due to non-trivial band structures are getting much attention.^[8-45] Among them, a ferromagnetic Weyl semimetal Co₂MnGa (CMG) with the $L2_1$ fully ordered Heusler structure shows the largest S_{ANE} value around room temperature.^[13,14,18,19,26] However, ANE in CMG has been measured mostly in single crystals ($S_{\text{ANE}} = 6.0 \sim 7.9 \mu\text{V K}^{-1}$)^[13,18,19] and epitaxial thin films ($S_{\text{ANE}} \sim 6.2 \mu\text{V K}^{-1}$),^[14, 26] which are not compatible to scalability and mass production.

For applications, polycrystalline slabs with large S_{ANE} are promising to construct low-cost and large-scale devices based on ANE.^[46-51] Owing to small anisotropy in the transport properties^[13] and robustness to the grain boundary scattering,^[47] giant ANE has been reported not only in the polycrystalline films^[34,43] but also in the polycrystalline slabs made by using a spark plasma sintering (SPS) method.^[46,47,50] SPS is a versatile pressure-assisted sintering method in short time and low energy cost, and thus useful for controlling the microstructure in polycrystalline thermoelectric materials to improve their thermoelectric performance.^[52-54] Furthermore, Ravi *et al.* demonstrated the remarkable change of S_{ANE} in Fe-based alloys by microstructure engineering.^[55] Therefore, the comprehensive understanding of the transport properties and detailed microstructure is crucial for the improvement of the performance of ANE in polycrystal materials for thermoelectric applications based on ANE.

In this study, we prepared polycrystalline CMG slabs with various sintering conditions using the SPS method and investigated their transport properties to optimize $z_{\text{ANE}}T$. The CMG slab sintered at a high temperature and high pressure exhibits $S_{\text{ANE}} \sim 7.5 \mu\text{V K}^{-1}$, which is comparable to the best value in the single- and poly-crystalline CMG slabs at room temperature. We also achieved the decrease of κ with maintaining sufficiently large σ and S_{ANE} , resulting in a record-high value of $z_{\text{ANE}}T$ around room temperature among all the bulk magnetic materials reported so far. We then performed detailed nano/microstructure analysis on the samples to clarify the influence of the nano/microstructure on the transport properties. The nano/microstructure analysis using transmission electron microscopy (TEM) revealed the importance of the crystal growth of the $L2_1$ ordered phase within the samples for showing large S_{ANE} even if its existence cannot be detected by the X-ray diffraction (XRD). In addition to the conventional $L2_1$ and $B2$ phases in CMG, we found an unknown crystal phase with a size of ten nanometers. This length scale coincides with the scale of mean free paths for phonons which mainly contribute to the thermal conductivity obtained by a first-principles calculation, suggesting that the nanometer-scale crystal boundaries increase the phonon scattering and cause small κ . Our results provide an insight into the correlation between the transport properties and nano/microstructures within the sample, which is important for the simultaneous optimization of ANE, electric conductivity, and thermal conductivity.

2. Results and Discussion

The polycrystalline CMG slabs were prepared under various sintering conditions from powder of CMG ingots. The detailed recipe for the preparation of CMG ingots is described in Experimental Section and Ref. 46. We crushed the CMG ingots using a mortar and planetary ball mill, followed by sieving the ball-milled CMG powder through a 63 μm mesh. An

inductively coupled plasma optical emission spectrometer determined the composition of the CMG powder to be $\text{Co}_{52.1}\text{Mn}_{23.1}\text{Ga}_{24.8}$. We loaded the CMG powder into a graphite die with a diameter of 10 mm and sintered it under various conditions. We examined nine sintering conditions combining three sintering temperatures of $T_{\text{sinter}} = 600, 700, \text{ and } 800^\circ\text{C}$ with three maximum sintering pressures of $p_{\text{max}} = 30, 60, \text{ and } 90 \text{ MPa}$. We kept T_{sinter} and p_{max} for 10 min in all the conditions. In the following, we define the sample name as $\text{CMG}(T_{\text{sinter}}, p_{\text{max}})$ for each sintering condition.

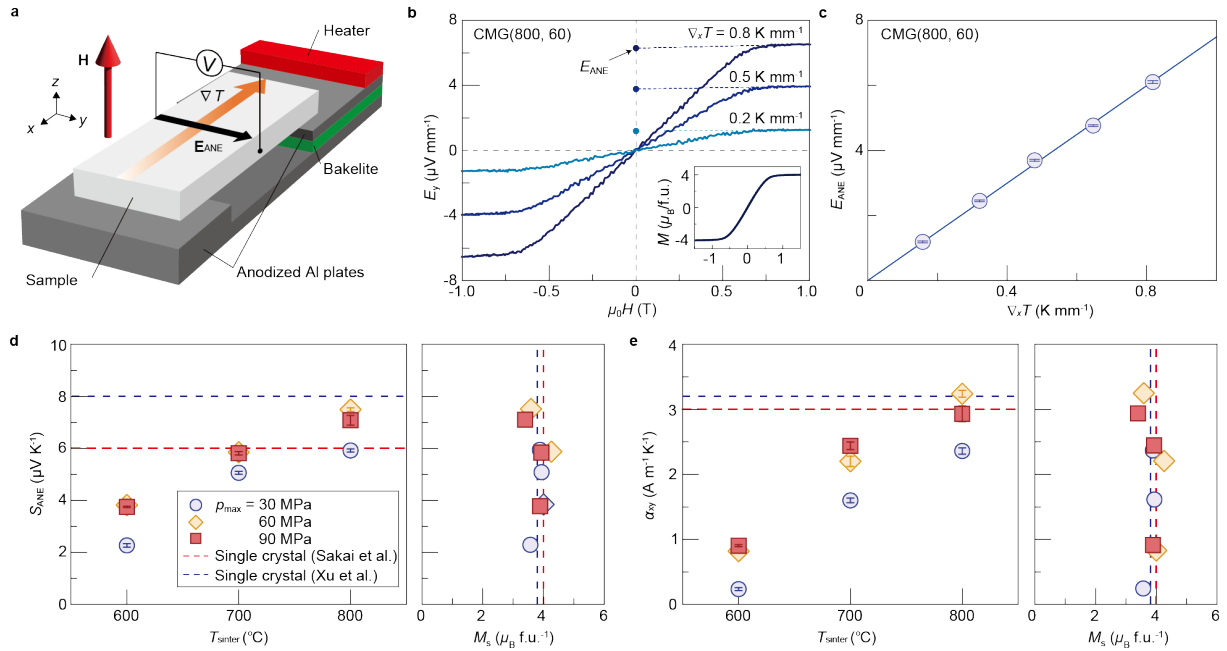


Figure 1. a) Schematic illustration of the measurement setup. b) H dependence of E_y in the CMG slab sintered at $T_{\text{sinter}} = 800^\circ\text{C}$ and $p_{\text{max}} = 60 \text{ MPa}$, i.e., CMG(800, 60), for various values of $\nabla_x T$. The inset to (b) shows the M - H curve of CMG(800, 60). The colored dashed lines in (b) show the linear extrapolation with the data in the high H region, where M is saturated (see the M - H curve), for estimating E_{ANE} represented as the colored dots at $\mu_0 H = 0$. c) $\nabla_x T$ dependence of E_{ANE} . The solid line in (c) shows the result of a linear fitting, of which the slope corresponds to S_{ANE} . d) T_{sinter} , p_{max} , and M_s dependences of S_{ANE} . e) T_{sinter} , p_{max} , and M_s dependences of α_{xy} . The red and blue dashed lines in (d) and (e) correspond to the S_{ANE} , α_{xy} , and M_s values obtained in the single-crystalline samples in Refs. 13 and 19, respectively.

We measured ANE at room temperature and atmospheric pressure using a homemade sample holder (**Figure 1a**). The sample holder consists of two anodized Al plates. The large one works as a thermal bath. The small one is equipped with a chip heater and is attached to the large one but thermally isolated from it by inserting a Bakelite board to create a temperature difference between the two plates. A sample was bridged between the plates and fixed using a high-thermal conductivity adhesive sheet. We generated a uniform temperature gradient ∇T in the x direction

and estimated the actual value of $\nabla_x T$ from a temperature-profile image at the surface of the sample coated with black ink using an infrared camera. We measured the thermoelectric voltage along the y direction V_y , i.e., the sample width direction, with the magnetic field \mathbf{H} along the out-of-plane direction and converted V_y into the transverse electric field $E_y = V_y/w = S_{\text{ANE}}\nabla_x T$, where w is the sample width.

Figure 1b shows the H dependence of E_y for CMG(800, 60) at different $\nabla_x T$ values. Clear E_y signals appear by applying $\nabla_x T$ and H . The magnitude of the E_y signal increases by increasing $\nabla_x T$ and its sign reverses with respect to the sign of H . By increasing $|H|$, the E_y signal is saturated at around $|\mu_0 H| \sim 0.8$ T, which is consistent with the saturation field of M (see the inset to Figure 1b), indicating that ANE mainly generates the E_y signal. In this setup, an H -linear signal due to the ordinary Nernst effect also appears. We subtracted the ordinary Nernst component by linear extrapolation for the results above the saturation field, represented as the colored dashed lines in Figure 1b, and obtained the ANE component E_{ANE} at $H = 0$ (see the colored dots). We estimated $S_{\text{ANE}} = E_{\text{ANE}}/\nabla_x T$ to be $\sim 7.5 \mu\text{V K}^{-1}$ for CMG(800, 60) by a linear fit to the $\nabla_x T$ dependence of E_{ANE} in Figure 1c. We obtained S_{ANE} for all the samples through the same procedure.

The left panel of Figure 1d summarizes the estimated S_{ANE} values in all the samples at room temperature. S_{ANE} monotonically increases by increasing T_{sinter} , and the relationship of S_{ANE} at the same T_{sinter} value is $\text{CMG}(T_{\text{sinter}}, 30) < \text{CMG}(T_{\text{sinter}}, 60) \sim \text{CMG}(T_{\text{sinter}}, 90)$. All the samples show relatively large S_{ANE} ($> 2 \mu\text{V K}^{-1}$), and the maximum S_{ANE} value of $7.5 \mu\text{V K}^{-1}$ in CMG(800, 60) is the largest among all the values previously reported in polycrystalline magnets including topological materials.^[6,7,34,35,39,43,45-47,55-58] More importantly, the maximum S_{ANE} value in the polycrystalline CMG slab is comparable to or even larger than that in the single-crystalline CMG slabs^[13,18,19] (see the blue and red dashed lines in the left panel of Figure 1d).

To further investigate large ANE in the polycrystalline CMG slabs, we estimated the anomalous Nernst conductivity α_{xy} . The left panel of Figure 1e shows the obtained α_{xy} values in all the samples using the formula $S_{\text{ANE}} = \rho_{xx}\alpha_{xy} - (\rho_{\text{AHE}}S_{\text{SE}}/\rho_{xx})$ with the measured longitudinal resistance ρ_{xx} , anomalous Hall resistivity ρ_{AHE} , and Seebeck coefficient S_{SE} (see Figure S1, Supporting Information). α_{xy} depends on the sintering condition and its trend is similar to that of S_{ANE} , while both S_{ANE} and α_{xy} are independent of the saturation magnetization M_s (see the right panels in Figure 1d and 1e). The maximum value of $\sim 3 \text{ A m}^{-1} \text{ K}^{-1}$ is comparable to that in the single-crystalline CMG samples.^[13,18,19] This indicates the crucial role of the Berry curvature and electronic band structure at the Fermi level even in the polycrystals in showing large S_{ANE} , consistent with the recent findings.^[34,35,39,41,43,45-46]

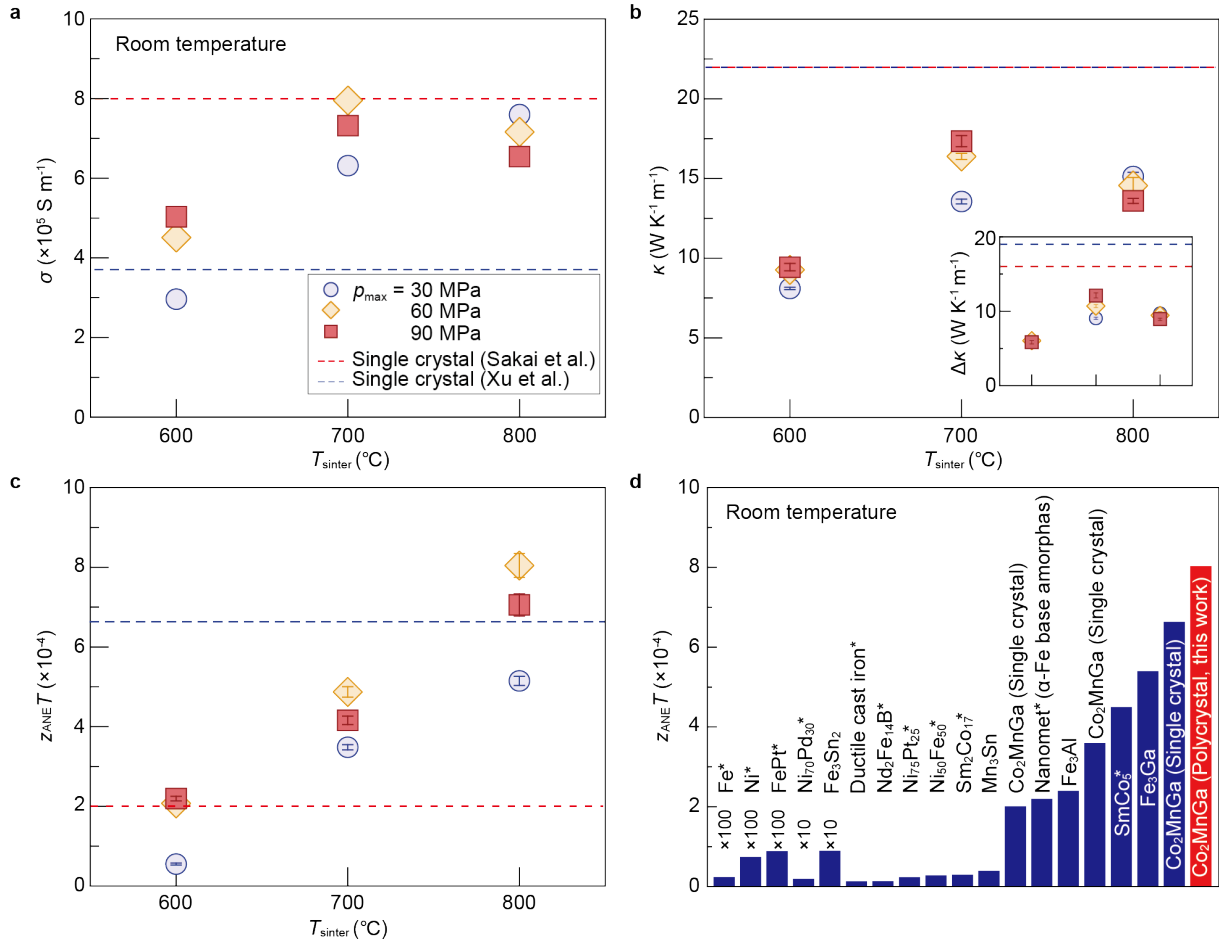


Figure 2. a-c) T_{sinter} and p_{max} dependences of σ (a), κ (b), and $z_{\text{ANE}}T$ (c) at room temperature ($T = 300$ K). The inset to (b) shows the T_{sinter} and p_{max} dependences of $\Delta\kappa$. The red and blue dashed lines in (a-c) correspond to the σ , κ , $\Delta\kappa$, and $z_{\text{ANE}}T$ values obtained in the single-crystalline samples in Refs. 13 and 19, respectively. d) Comparison of $z_{\text{ANE}}T$ between our polycrystalline CMG slab (red bar) and the various bulk magnets (blue bars) around room temperature. $z_{\text{ANE}}T$ for the materials with an asterisk are estimated using the experimental results of the anomalous Ettingshausen effect and the Onsager reciprocal relation.

We next focus on $z_{\text{ANE}}T$ to discuss the transverse thermoelectric performance of the polycrystalline CMG slabs. σ and κ , which is obtained using the density, specific heat, and thermal diffusivity (see Figure S2, Supporting Information), for all the samples are summarized in **Figure 2a** and **2b**. We found that σ and κ of the samples prepared at $T_{\text{sinter}} = 700^\circ\text{C}$ and 800°C are larger than those of the sample prepared at $T_{\text{sinter}} = 600^\circ\text{C}$. Although σ of the samples prepared at $T_{\text{sinter}} = 700^\circ\text{C}$ and 800°C is comparable to that of the single-crystalline CMG samples, κ is about 25% smaller than that of the single crystal.^[19] This indicates that we successfully reduced κ without decrease of σ and S_{ANE} , which is important for improving $z_{\text{ANE}}T$ (see Equation 1). Figure 2c shows the sintering condition dependence of $z_{\text{ANE}}T$ for all the

samples, which is estimated from the results in Figure 1d, 2a, and 2b. The overall trend is determined primarily by S_{ANE} . The CMG(800, 60) sample shows the maximum value of $\sim 8.0 \times 10^{-4}$, which is surprisingly greater than that for the single-crystalline CMG slab ($z_{\text{ANE}}T \sim 2.0 \times 10^{-4}$ in Ref. 13 and $\sim 6.6 \times 10^{-4}$ in Ref. 19 shown as the red and blue dashed lines, respectively). Furthermore, this value is much larger than $z_{\text{ANE}}T$ in other magnetic materials exhibiting large ANE, such as the single-crystalline Fe_3Ga slab^[22] and the polycrystalline SmCo_5 -type permanent magnets,^[6] summarized in Figure 2d.^[12,13,18,19,22,32,55-58]

Now, we consider the origin of the high-performance of ANE in the sintered CMG slabs. We found that the samples sintered at $T_{\text{sinter}} = 600^\circ\text{C}$ and 700°C have a lower relative density, the ratio of the measured density to the theoretical density, than that of the samples sintered at 800°C (see Figure S2, Supporting Information) and a rough surface with remaining pores and microparticles (characterized by ultra-low voltage SEM as shown in Figure S3, Supporting Information). These indicate that the samples sintered at lower T_{sinter} are insufficiently densified, resulting in small S_{ANE} in CMG(600, p_{max}) and CMG(700, 30). In fact, the CMG ingot annealed at 600°C with the relative density nearly of 100% exhibits S_{ANE} of $5.4 \mu\text{V K}^{-1}$, which is much larger than that of the insufficiently densified CMG(600, p_{max}) ($S_{\text{ANE}} = 2 \sim 4 \mu\text{V K}^{-1}$), suggesting the correlation between S_{ANE} and the relative density, rather than the exposed temperature. On the other hand, although both CMG(800, 30) and CMG(800, 90) show the relative density of nearly 100% and dense morphology, CMG(800, 90) shows larger S_{ANE} than CMG(800, 30), indicating that the difference in the sample density cannot explain large ANE in CMG(800, 90). Therefore, to understand the origin of large S_{ANE} in CMG(800, 90), we performed the micro- and nano-scale structure analysis, i.e., SEM, energy dispersive X-ray spectrometry (EDS), and high-resolution high-angle annular dark field (HAADF) scanning transmission electron microscopy (STEM), on two samples.

Figure 3a shows the SEM-EDS maps of Co, Mn, and Ga for the CMG(800, 90) and CMG(800, 30) slabs. We found an inhomogeneous distribution of Mn in both samples where Mn segregation can be seen at the surface of particles close to the grain boundary region. In both samples, the typical grain size is comparable (a few to several tens of micrometers). This grain size is consistent with the size of the initial powder of CMG, which was sieved through a $63 \mu\text{m}$ mesh.

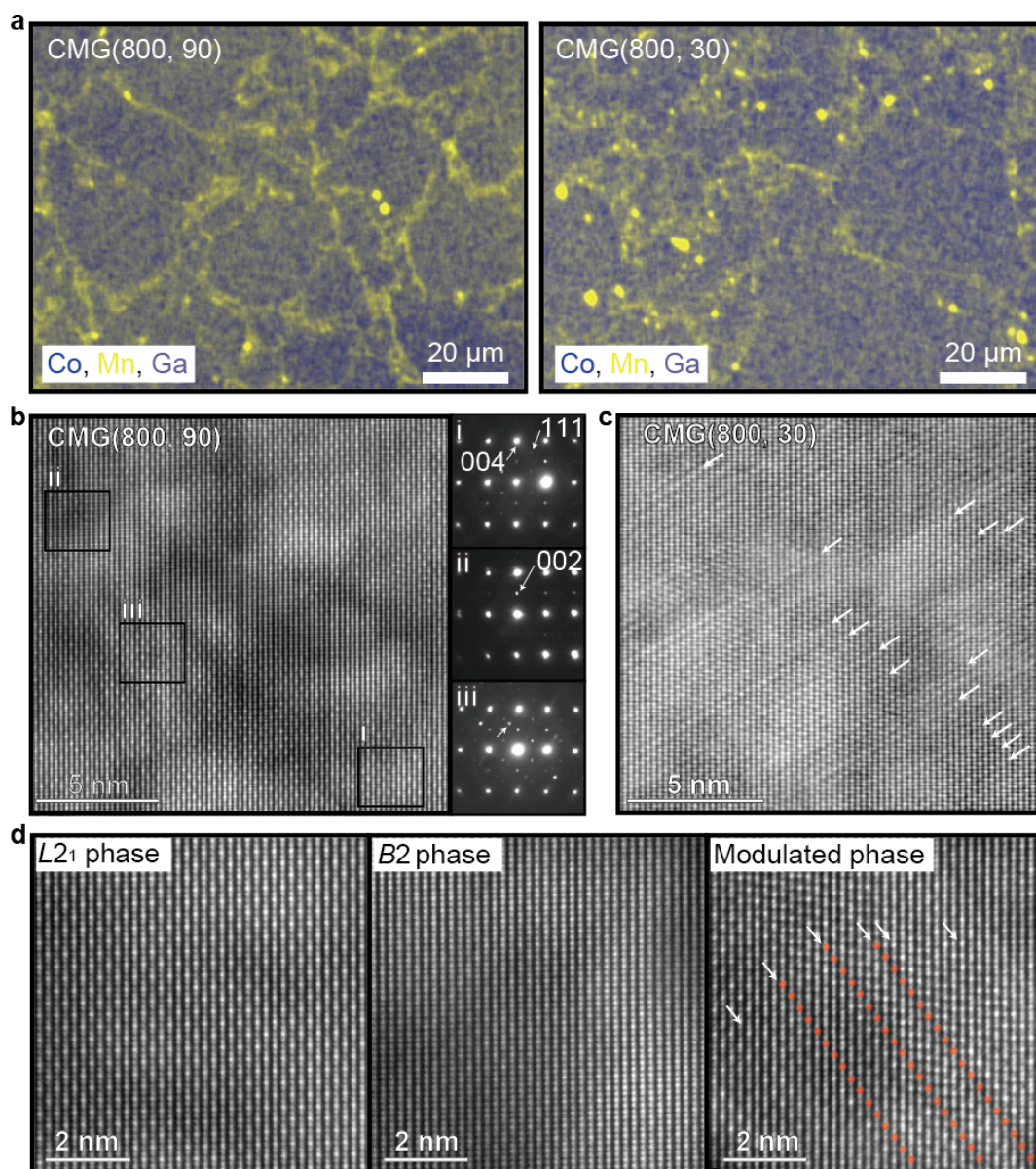


Figure 3. a) SEM-EDS maps for CMG(800, 90) (left panel) and CMG(800, 30) (right panel). b) High-resolution HAADF-STEM image obtained from CMG(800, 90) and electron-beam diffraction patterns obtained from the labelled regions. c) High-resolution HAADF-STEM image from CMG(800, 30). d) High magnification HAADF-STEM images showing the $L2_1$, $B2$, and modulated phases.

Figure 3b, 3c and 3d show high resolution HAADF-STEM images and nano-beam electron diffraction patterns obtained from CMG(800, 90) and CMG(800, 30). Although the bulk XRD patterns show only fundamental diffraction peaks of the $A2$ phase (Figure S4, Supporting Information), the nano-beam diffraction patterns in the i and ii regions in Figure 3b indicate the presence of the $L2_1$ and $B2$ ordered phases by 111 and 002 superlattice reflections in the diffraction patterns obtained along [111] zone axis of matrix phase, respectively, indicating that the ordered structure of CMG(800, 90) varies in the nanoscale containing. We found that the

electron beam diffraction pattern in the iii region is different from that of both $L2_1$ and $B2$ phases; an additional superlattice reflection appears diagonally on either side of the 002 spot indicated by the white arrows in the bottom of the right panels of Figure 3b. To closely see the crystal structure of this unconventional modulated phase, we show the magnified HAADF-STEM images for the $L2_1$, $B2$, and modulated phases in Figure 3d. In comparison with the $L2_1$ and $B2$ structures, the modulated phase consists of the relatively displaced atoms in the diagonal direction (see red colored dots indicated by the white arrows in the right panel of Figure 3d), similar to a martensite. Although the TEM observation gives the local information, CMG(800, 30) seems to have a larger amount of the modulated phase than CMG(800, 90) (see the lines of the displaced atoms indicated by the white arrows in Figure 3c), suggesting that the increase of the sintering pressure at high sintering temperature facilitates the transformation of the modulated phase into the $L2_1$ and/or $B2$ phases.

We also found clear difference between CMG(800, 30) and CMG(800, 90) in the M - T curves shown in **Figure 4**. A large thermal hysteresis appears in CMG(800, 30) within the T range from 500 K to 750 K, while it almost disappears in CMG(800, 90). The observed thermal hysteresis is irrelevant to the magnetic ordering transition because M appears at around 800 K. The onset temperature of M for CMG(800, 90) is lower than CMG(800, 30), and CMG(800, 30) shows larger M than CMG(800, 90). A similar thermal hysteresis has been observed in the thin film of CMG^[59] and other Heusler alloys with the martensitic transformations caused by the distortion of the crystal structure.^[60-62] In our case, the observed martensitic-transformation-like hysteresis can be caused by the diagonal displacement of the atoms in the modulated phase (see Figure 3d). Although determination of the actual Curie temperature is difficult in our case due to the application of the large magnetic field, the onset temperature of M at 1 T for CMG(800, 90) is closer to the literature Curie temperature for $L2_1$ -type CMG (~ 685 K)^[63] than that for CMG(800, 30). By measuring the M - T curves at 1 T at low temperatures (see the inset to Figure 4), we obtained M_s at $T = 5$ K for CMG(800, 30) as $4.2 \mu_B \text{ f.u.}^{-1}$ and CMG(800, 90) as $4.1 \mu_B \text{ f.u.}^{-1}$. CMG(800, 90) shows M_s consistent with the experimental and theoretical values for $L2_1$ -type CMG ($\sim 4.1 \mu_B \text{ f.u.}^{-1}$)^[63,64] and closer to the experimental value for the $B2$ -type CMG film at 4.2 K ($\sim 3 \mu_B \text{ f.u.}^{-1}$)^[65] than that for CMG(800, 30). All the results indicate that the magnetic properties of CMG(800, 90) are more similar to those of $L2_1/B2$ -type CMG than those of CMG(800, 30), suggesting the transformation from the modulated phase into the $L2_1$ and/or $B2$ phases. This interpretation is consistent with the TEM observation. Therefore, the sintering pressure at high sintering temperature affects the degree of the crystalline orders in the samples.

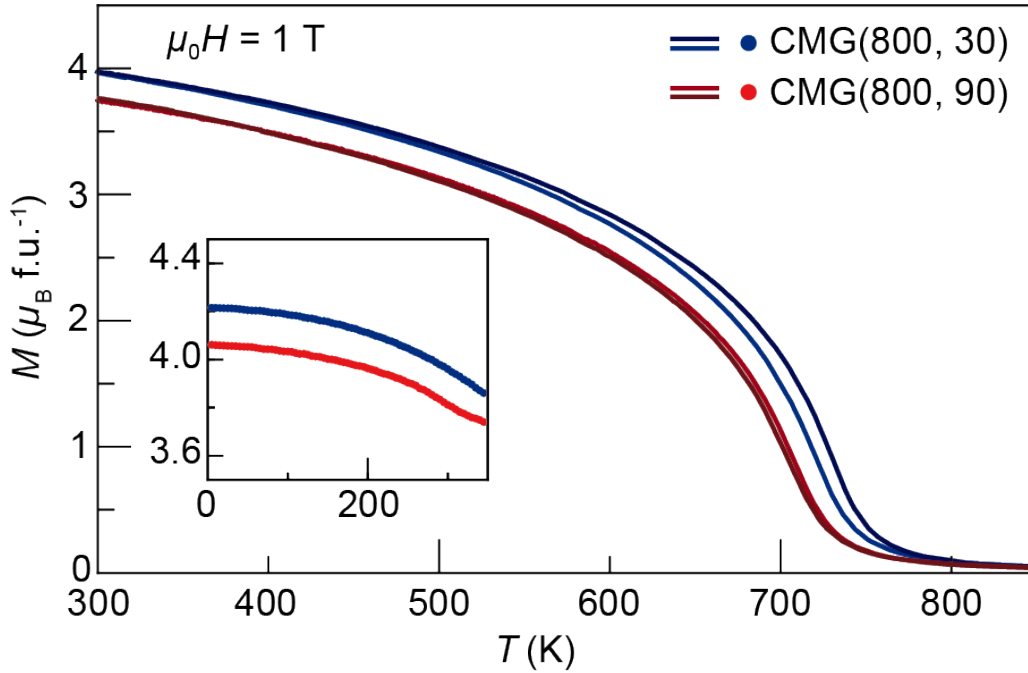


Figure 4. T dependence of M for CMG(800, 30) and CMG(800, 90) at $\mu_0 H = 1$ T. The inset shows the averaged values of M in the T range from 5 K to 350 K.

The above results confirm that the degree of the crystalline order is important for obtaining large S_{ANE} .^[21,66,67] We found that CMG(800, 90) exhibits the larger value of S_{ANE} than that in CMG(800, 30), which has more modulated phase than the $L2_1$ and/or $B2$ phases. Because the theoretical origin of large ANE in CMG is the topological electronic band structure in the fully ordered $L2_1$ phase,^[13,18,66] our results suggest that ANE in the modulated phase seems to be small, and thus the reduction of the modulated phase is crucial for obtaining large S_{ANE} .

Now, we focus on the reduction of κ in CMG(800, 30) and CMG(800, 90). The inset to Figure 2b shows the sintering condition dependence of the nonelectronic thermal conductivity $\Delta\kappa = \kappa - \kappa_{\text{el}}$, where the electronic thermal conductivity κ_{el} is estimated via the Wiedemann-Franz law with the free-electron Lorenz number of $2.44 \times 10^{-8} \text{ W } \Omega \text{ K}^{-2}$. Since the values of σ in CMG(800, 30) and CMG(800, 90) are comparable to that in the single crystal^[19] (see Figure 2a), κ_{el} does not contribute to the decrease of κ in our samples. On the other hand, we found the sizable decrease in $\Delta\kappa$ compared with the single crystal's value (represented as the dotted lines). Phonon and magnon can contribute to $\Delta\kappa$ in magnetic materials.^[68] However, we assumed the magnon contribution is negligibly small in CMG at room temperature because the experimental observation of magnon contribution has been typically at very low temperatures^[69,70] and the magnetic damping constant of the polycrystalline CMG^[71] is one order of magnitude larger than that of CoFe alloys which show measurable magnon contribution at room temperature.^[72]

Therefore, the thermal conductivity carried by phonons plays an important role in the decrease of κ .

A plausible mechanism of the decrease of $\Delta\kappa$ is the increase of phonon-boundary scattering caused by nano/microstructure.^[52-54] To investigate the phonon thermal conductivity κ_{ph} , we carried out a first-principles calculation, whose details are described in Experimental Section, with taking 3- and 4-phonon, and isotope scatterings into account and obtained cumulative κ_{ph} , which provides a useful insight into the reduction of κ_{ph} by nano/microstructures. **Figure 5a** shows cumulative κ_{ph} as a function of the phonon mean free path L for CMG at room temperature. Cumulative κ_{ph} rapidly increases from $L \sim 10$ nm and is saturated to ~ 23 W K⁻¹ m⁻¹ above $L > 1$ μm . The saturation value is comparable to the value of κ in the single crystal and much larger than that in our samples. Our calculation indicates that phonons with L in the range from 10 nm to 100 nm mainly carry heat in CMG, and scattering centers with the size of such the scale can efficiently reduce κ_{ph} . However, this length scale is much smaller than the typical grain size with the order of 10 μm in both CMG(800, 30) and CMG(800, 90) shown in the SEM images in Figure 5b (Figure S3, Supporting Information, showing the SEM images for all the samples). We ignored phonon-electron and phonon-magnon scatterings in the calculation. They increase the phonon scattering and play an important role for quantitative discussion on κ , but only make the length scale of the heat-carrying phonons shorter. Therefore, even when phonon-electron and phonon-magnon scatterings are taken into account, the grains of the order of 10 μm in size cannot be responsible for the decrease in $\Delta\kappa$ due to the phonon-boundary scatterings. On the other hand, recall that the CMG samples contain the crystal phase separation in the nanometer scale, as observed in Figure 3b-d. The coincidence between L of the heat-carrying phonons and the size of the crystal phase separation indicates that the crystal-domain boundary induces phonon scatterings, resulting in the decrease of $\Delta\kappa$. Our results suggest that phonon engineering using not only grain boundaries but also crystal-domain boundaries can increase the performance of thermoelectric materials.

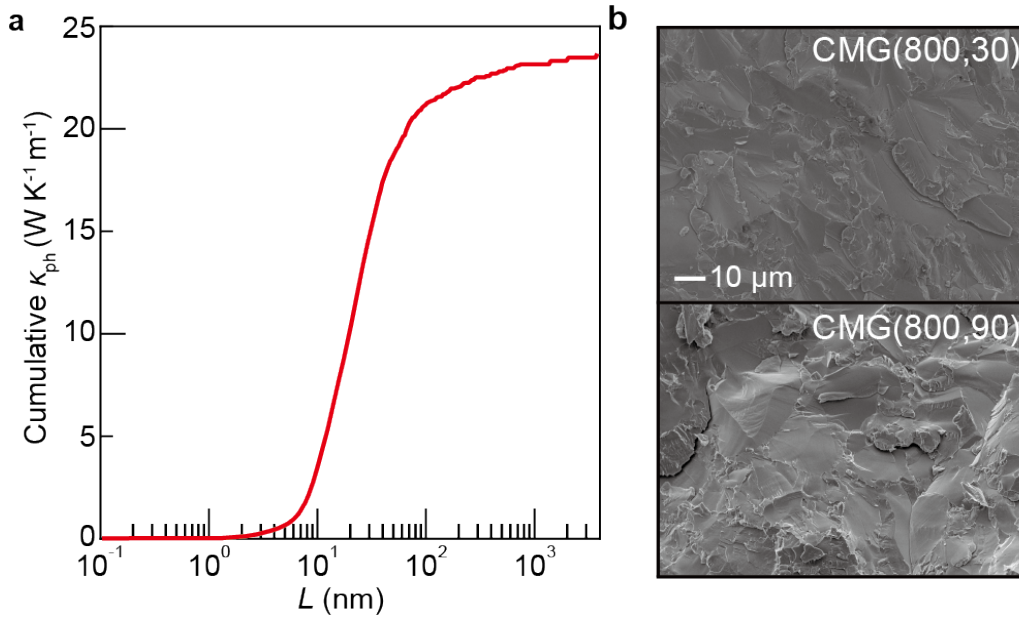


Figure 5. a) Calculation of cumulative κ_{ph} for CMG as a function of L at $T = 300 \text{ K}$. b) SEM images of the fracture surface of CMG(800, 30) and CMG(800, 90).

3. Conclusion

In summary, we investigated ANE at room temperature in polycrystalline CMG slabs prepared by the SPS method in various sintering conditions. The maximum values of S_{ANE} and α_{xy} of our polycrystalline CMG slabs prepared at a high sintering temperature and pressure are comparable to those in the single-crystalline CMG slab and are largest at room temperature among polycrystalline magnetic materials. Furthermore, the optimized CMG slab achieved the record-high $z_{\text{ANE}}T$ value of 8×10^{-4} at room temperature, which is larger than that for the single-crystalline CMG samples, owing to the decrease of κ . The transport measurements and nano/microstructure analysis indicate that the degree of the crystalline order is important for obtaining large S_{ANE} . Based on the calculation of the phonon transport spectrum and nanoscale structure analysis, we suggest the importance of the crystal-domain boundary for increasing phonon scatterings to decrease $\Delta\kappa$ and κ , which is a different strategy of the conventional phonon engineering using grain boundaries to increase phonon scatterings. Our results demonstrate that the integration of approaches used for development of the conventional thermoelectric materials,^[73] e.g., phonon engineering, nano-structuring, and fabricating bulk composite, will be also important to improve the performance of the magneto-thermoelectric devices.

4. Experimental Section

Sample Preparation: The ingot of CMG was prepared from the stoichiometric amount of Co (99.7% purity), Mn (99.99% purity), and Ga (99.9999% purity), comically obtained from Rare Metallic Co., Ltd., using an arc-melting method in an Ar atmosphere. The obtained ingot was annealed in a high vacuum at 1000°C for 48 h and subsequently at 600°C for 72 h for homogenization. The CMG ingot was crushed using a mortar and planetary ball mill, and the ball-milled CMG powder was sieved through a 63 μm mesh. The CMG powder was loaded in a graphite die with a diameter of 10 mm and sintered under various conditions described in the main text using Dr. Sinter Lab Jr. (Fuji Electronic Industrial Co., Ltd.). The sintered CMG slabs were cut into a rectangular shape with a length of 9-10 mm, width of 2 mm, and thickness of 0.4-0.9 mm for measuring the transport properties and magnetization M , and into a disc with a diameter of 10 mm and thickness of 1 mm for measuring the thermal diffusivity, using a diamond wire saw. Note that the variation in the shape of the rectangular samples does not affect the measurement results.

Material and Microstructure Characterization: The longitudinal electric conductivity and Seebeck coefficient were measured using a Seebeck Coefficient/Electric Resistance Measurement System (ZEM-3, Advance Riko, Inc.). The anomalous Hall effect was measured in the same setup for the ANE measurement, where a charge current was applied instead of the thermal gradient. To determine the thermal conductivity, the thermal diffusivity, specific heat, and density were measured using the laser flash method, differential scanning calorimetry, and Archimedes method, respectively. The temperature dependence of the magnetization was measured under the magnetic field of 1 T in the temperature range from 300 K to 850 K using a superconducting quantum interference device equipped with a vibrating sample magnetometer (SQUID-VSM, Quantum Design) and from 5 K to 350 K using a superconducting quantum interference device (SQUID) magnetometer (MPMS-5L, Quantum Design), respectively. The surfaces of the samples were observed using an ultra-low voltage SEM JSM-7800F Prime (Jeol Ltd.). Microstructure of the samples was investigated by scanning electron microscopy (SEM) using a Cross-Beam 1540ESB (Carl Zeiss). Scanning transmission electron microscopy (STEM) was conducted using a Titan G2 80-200 (FEI) with a probe aberration corrector. The lift-out method was used to prepare the TEM specimens using a focused ion beam system Helios G4-UX DualBeam (FEI).

First Principle Phonon Calculation: The phonon thermal conductivity κ_{ph} of the $L2_1$ ordered CMG was calculated based on Peierls-Boltzmann theory (PBT) within the single-mode relaxation time approximation, as implemented in the ALAMODE code.^[75] The calculations considered the 3-phonon, 4-phonon, and phonon-isotope scattering processes. The harmonic, cubic, and quartic interatomic force constants (IFCs) necessary for the scattering probability calculations were estimated by linear regression,^[74] where the IFCs were fitted to the displacement-force datasets obtained from DFT calculations. For harmonic IFCs, an atom in the $2 \times 2 \times 2$ conventional supercell (128 atoms in total) was displaced from its original position by 0.01 Å, and forces were computed using the *Vienna Ab initio Simulation Package* (VASP).^[76,77] For the anharmonic IFCs, 40 random atomic configurations sampled from the distribution function of the quantum harmonic oscillator at 300 K were used. We computed all symmetrically inequivalent harmonic IFCs in the supercell. For the anharmonic IFCs, we included onsite, two-body, and three-body terms within the fifth-nearest neighbor shells, with which we confirmed the convergence of κ_{ph} . The PBT and three-phonon scattering rate calculations were performed using a $40 \times 40 \times 40$ uniform grid in the first Brillouin zone, whereas the four-phonon scattering rates were computed using a coarser $20 \times 20 \times 20$ and subsequently interpolated to the $40 \times 40 \times 40$ via a log-linear interpolation method. All the supercell VASP calculations were conducted with a kinetic energy cutoff of 500 eV, a $4 \times 4 \times 4$ Monkhorst-Pack grid for the Brillouin zone sampling, and a convergence criterion of 10^{-8} eV for the self-consistent-field iteration. For the exchange-correlation term, the Perdew-Burke-Ernzerhof functional^[78] within the generalized gradient approximation (GGA-PBE) was used. We used the DFT-optimized lattice constant with the collinear ferromagnetic spin configuration and neglected the spin-orbit interaction throughout calculations.

Supporting Information

Supporting Information is available from the Wiley Online Library or from the author.

Acknowledgements

The authors thank M. Isomura and K. Suzuki for technical supports, and S. J. Park for fruitful discussion. This work was supported by JST CREST “Creation of Innovative Core Technologies for Nano-enabled Thermal Management” (JPMJCR17I1), JST ERATO “Magnetic Thermal Management Materials” (JPMJER2201), JSPS KAKENHI Grant-in-Aid for Early-Career Scientists (21K14519), JSPS KAKENHI Grant-in-Aid for Scientific Research

(S) (22H04965), NEC Corporation, and NIMS Joint Research Hub Program. The computations in the present work were performed using the Numerical Materials Simulator at NIMS.

Conflict of Interest

The authors have no conflicts to disclose.

Data Availability Statement

The data that support the findings of this study are available from the corresponding author upon reasonable request.

Received: ((will be filled in by the editorial staff))

Revised: ((will be filled in by the editorial staff))

Published online: ((will be filled in by the editorial staff))

References

- [1] C. Fu, Y. Sun, C. Felser, *APL Mater.* **2020**, *8*, 040913.
- [2] K. Uchida, W. Zhou, Y. Sakuraba, *Appl. Phys. Lett.* **2021**, *118*, 140504.
- [3] K. Uchida, *Proc. Jpn. Acad., Ser. B* **2021**, *97*, 69.
- [4] K. Uchida, J. P. Heremans, *Joule* **2022**, *6*, 2240.
- [5] K. Uchida, H. Adachi, T. Kikkawa, A. Kirihara, M. Ishida, S. Yorozu, S. Maekawa, E. Saitoh, *Proc. IEEE* **2016**, *104*, 1946.
- [6] A. Miura, H. Sepehri-Amin, K. Masuda, H. Tsuchiura, Y. Miura, R. Iguchi, Y. Sakuraba, J. Shiomi, K. Hono, K. Uchida, *Appl. Phys. Lett.* **2019**, *115*, 222403.
- [7] A. Miura, K. Masuda, T. Hirai, R. Iguchi, T. Seki, Y. Miura, H. Tsuchiura, K. Takanashi, K. Uchida, *Appl. Phys. Lett.* **2020**, *117*, 082408.
- [8] D. Xiao, Y. Yao, Z. Fang, Q. Niu, *Phys. Rev. Lett.* **2006**, *97*, 026603.
- [9] T. Miyasato, N. Abe, T. Fujii, A. Asamitsu, S. Onoda, Y. Onose, N. Nagaosa, Y. Tokura, *Phys. Rev. Lett.* **2007**, *99*, 086602.
- [10] Y. Pu, D. Chiba, F. Matsukura, H. Ohno, J. Shi, *Phys. Rev. Lett.* **2008**, *101*, 117208.
- [11] M. Ikhlas, T. Tomita, T. Koretsune, M. Suzuki, D. Nishio-Hamane, R. Arita, Y. Otani, S. Nakatsuji, *Nat. Phys.* **2017**, *13*, 1085.
- [12] X. Li, L. Xu, L. Ding, J. Wang, M. Shen, X. Lu, Z. Zhu, K. Behnia, *Phys. Rev. Lett.* **2017**, *119*, 056601.

- [13] A. Sakai, Y. P. Mizuta, A. A. Nugroho, R. Sihombing, T. Koretsune, M. Suzuki, N. Takemori, R. Ishii, D. Nishio-Hamane, R. Arita, P. Goswami, S. Nakatsuji, *Nat. Phys.* **2018**, *14*, 1119.
- [14] H. Reichlova, R. Schlitz, S. Beckert, P. Swekis, A. Markou, Y.-C. Chen, D. Kriegner, S. Fabretti, G. H. Park, A. Niemann, S. Sudheendra, A. Thomas, K. Nielsch, C. Felser, S. T. B. Goennenwein, *Appl. Phys. Lett.* **2018**, *113*, 212405.
- [15] J. Hu, B. Ernst, S. Tu, M. Kuveždić, A. Hamzić, E. Tafra, M. Basletić, Y. Zhang, A. Markou, C. Felser, A. Fert, W. Zhao, J.-P. Ansermet, H. Yu, *Phys. Rev. Appl.* **2018**, *10*, 044037.
- [16] C. Wuttke, F. Cagliaris, S. Sykora, F. Scaravaggi, A. U. B. Wolter, K. Manna, V. Süß, C. Shekhar, C. Felser, B. Büchner, C. Hess, *Phys. Rev. B* **2019**, *100*, 085111.
- [17] S. N. Guin, P. Vir, Y. Zhang, N. Kumar, S. J. Watzman, C. Fu, E. Liu, K. Manna, W. Schnelle, J. Gooth, C. Shekhar, Y. Sun, C. Felser, *Adv. Mater.* **2019**, *31*, 1806622.
- [18] S. N. Guin, K. Manna, J. Noky, S. J. Watzman, C. Fu, N. Kumar, W. Schnelle, C. Shekhar, Y. Sun, J. Gooth, C. Felser, *NPG Asia Mater.* **2019**, *11*, 16.
- [19] L. Xu, X. Li, L. Ding, T. Chen, A. Sakai, B. Fauqué, S. Nakatsuji, Z. Zhu, K. Behnia, *Phys. Rev. B* **2020**, *101*, 180404(R).
- [20] C. D. W. Cox, A. J. Caruana, M. D. Cropper, K. Morrison, *J. Phys. D: Appl. Phys.* **2020**, *53*, 035005.
- [21] Y. Sakuraba, K. Hyodo, A. Sakuma, S. Mitani, *Phys. Rev. B* **2020**, *101*, 134407.
- [22] A. Sakai, S. Minamis, T. Koretsune, T. Chen, T. Higo, Y. Wang, T. Nomoto, M. Hirayama, S. Miwa, D. Nishio-Hamane, F. Ishii, R. Arita, S. Nakatsuji, *Nature* **2020**, *581*, 53.
- [23] R. Kraft, S. Srichandan, G. Fischer, C. Sürgers, *J. Appl. Phys.* **2020**, *128*, 033905.
- [24] G.-H. Park, H. Reichlova, R. Schlitz, M. Lammel, A. Markou, P. Swekis, P. Ritzinger, D. Kriegner, J. Noky, J. Gayles, Y. Sun, C. Felser, K. Nielsch, S. T. B. Goennenwein, A. Thomas, *Phys. Rev. B* **2020**, *101*, 060406(R).
- [25] D. Khadka, T. R. Thapaliya, S. H. Parra, J. Wen, R. Need, J. M. Kikkawa, S. X. Huang, *Phys. Rev. Mater.* **2020**, *4*, 084203.
- [26] K. Sumida, Y. Sakuraba, K. Masuda, T. Kono, M. Kakoki, K. Goto, W. Zhou, K. Miyamoto, Y. Miura, T. Okuda, A. Kimura, *Commun. Mater.* **2020**, *1*, 89.
- [27] S. Deng, R. Kraft, G. Fischer, C. Sürgers, *Appl. Phys. Lett.* **2020**, *117*, 262402.
- [28] H. Yang, W. You, J. Wang, J. Huang, C. Xi, X. Xu, C. Cao, M. Tian, Z.-A. Xu, J. Dai, Y. Li, *Phys. Rev. Mater.* **2020**, *4*, 042202.
- [29] T. Asaba, V. Ivanov, S. M. Thomas, S. Y. Savrasov, J. D. Thompson, E. D. Bauer, F. Ronning, *Sci. Adv.* **2021**, *7*, eabf1467.

- [30] F. Mende, J. Noky, S. N. Guin, G. H. Fecher, K. Manna, P. Adler, W. Schnelle, Y. Sun, C. Fu, C. Felser, *Adv. Sci.* **2021**, *8*, 2100782.
- [31] . Xu, L. Das, J. Z. Ma, C. J. Yi, S. M. Nie, Y. G. Shi, A. Tiwari, S. S. Tsirkin, T. Neupert, M. Medarde, M. Shi, J. Chang, T. Shang, *Phys. Rev. Lett.* **2021**, *126*, 076602.
- [32] H. Zhang, C. Q. Xu, X. Ke, *Phys. Rev. B* **2021**, *103*, L201101.
- [33] Y. Pan, C. Le, B. He, S. J. Watzman, M. Yao, J. Gooth, J. P. Heremans, Y. Sun, C. Felser, *Nat. Mater.* **2022**, *21*, 203.
- [34] Wang, Y.-K. Lau, W. Zhou, T. Seki, Y. Sakuraba, T. Kubota, K. Ito, K. Takanashi, *Adv. Electron. Mater.* **2022**, *8*, 2101380.
- [35] Z. Feng, S. Minami, S. Akamatsu, A. Sakai, T. Chen, D. Nishio-Hamane, S. Nakatsuji, *Adv. Funct. Mater.* **2022**, *32*, 2206519.
- [36] Y. You, H. Lam, C. Wan, C. Wan, W. Zhu, L. Han, H. Bai, Y. Zhou, L. Qiao, T. Chen, F. Pan, J. Liu, C. Song, *Phys. Rev. Appl.* **2022**, *18*, 024007.
- [37] H. Zhang, J. Koo, C. Xu, M. Sretenovic, B. Yan, X. Ke, *Nat. Commun.* **2022**, *13*, 1091.
- [38] S. Roychowdhury, A. M. Ochs, S. N. Guin, K. Samanta, J. Noky, C. Shekhar, M. G. Vergniory, J. E. Goldberger, C. Felser, *Adv. Mat.* **2022**, *34*, 2201350.
- [39] T. Chen, S. Minami, A. Sakai, Y. Wang, Z. Feng, T. Nomoto, M. Hirayama, R. Ishii, T. Koretsune, R. Arita, S. Nakatsuji, *Sci. Adv.* **2022**, *8*, eabk1480.
- [40] S. Roychowdhury, M. Yao, K. Samanta, S. Bae, D. Chen, S. Ju, A. Raghavan, N. Kumar, P. Constantinou, S. N. Guin, N. C. Plumb, M. Romanelli, H. Borrmann, M. G. Vergniory, V. N. Strocov, V. Madhavan, C. Shekhar, C. Felser, *Adv. Sci.* **2023**, *10*, 2207121.
- [41] K. Fujiwara, Y. Kato, H. Abe, S. Noguchi, J. Shiogai, Y. Niwa, H. Kumigashira, Y. Motome, A. Tsukazaki, *Nat. Commun.* **2023**, *14*, 3399.
- [42] M. Li, H. Pi, Y. Zhao, T. Lin, Q. Zhang, X. Hu, C. Xiong, Z. Qiu, L. Wang, Y. Zhang, J. Cai, W. Liu, J. Sun, F. Hu, L. Gu, H. Weng, Q. Wu, S. Wang, Y. Chen, B. Shen, *Adv. Mat.* **2023**, *35*, 2301339.
- [43] R. Uesugi, T. Higo, S. Nakatsuji, *Appl. Phys. Lett.* **2023**, *123*, 252401.
- [44] S. Noguchi, K. Fujiwara, Y. Yanagi, M. Suzuki, T. Hirai, T. Seki, K. Uchida, A. Tsukazaki, *Nat. Phys.* **2024**, *20*, 254.
- [45] Y. Wang, A. Sakai, S. Minami, H. Gu, T. Chen, Z. Feng, D. Nishio-Hamane, S. Nakatsuji, *Appl. Phys. Lett.* **2024**, *125*, 081901.
- [46] W. Zhou, A. Miura, T. Hirai, Y. Sakuraba, K. Uchida, *Appl. Phys. Lett.* **2023**, *122*, 062402.
- [47] M. Chen, J. Wang, K. Liu, W. Fan, Y. Sun, C. Felser, T. Zhu, C. Fu, *Adv. Energy Mater.* **2024**, *14*, 2400411.

- [48] K. Uchida, T. Hirai, F. Ando, H. Sepehri-Amin, *Adv. Energy Mater.* **2024**, *14*, 2302375.
- [49] F. Ando, T. Hirai, K. Uchida, *APL Energy* **2024**, *2*, 016103.
- [50] T. Hirai, F. Ando, H. Sepehri-Amin, K. Uchida, *Nat. Commun.* **2024**, *15*, 9643.
- [51] F. Ando, T. Hirai, A. Alasli, H. Sepehri-Amin, Y. Iwasaki, H. Nagano, K. Uchida, (*Preprint*) *arXiv*, 2402.18019, ver2, submitted: July, **2024**.
- [52] A. J. Minnich, M. S. Dresselhaus, Z. F. Ren, G. Chen, *Energy Environ. Sci.* **2009**, *2*, 466.
- [53] M. Nomura, J. Shiomi, T. Shiga, R. Anufriev, *Jpn. J. Appl. Phys.* **2018**, *57*, 080101.
- [54] S. I. Kim, K. H. Lee, H. A. Mun, H. S. Kim, S. W. Hwang, J. W. Roh, D. J. Yang, W. H. Shin, X. S. Li, Y. H. Lee, G. J. Snyder, S. W. Kim, *Science* **2015**, *348*, 109.
- [55] R. Gautam, T. Hirai, A. Alasli, H. Nagano, T. Ohkubo, K. Uchida, H. Sepehri-Amin, *Nat. Commun.* **2024**, *15*, 2184.
- [56] E. H. Butler, Jr., E. M. Pugh, *Phys. Rev.* **1940**, *57*, 916.
- [57] A. Miura, R. Iguchi, T. Seki, K. Takanashi, K. Uchida, *Phys. Rev. Mater.* **2020**, *4*, 034409.
- [58] R. Nagasawa, K. Oyanagi, T. Hirai, R. Modak, S. Kobayashi, K. Uchida, *Appl. Phys. Lett.* **2022**, *121*, 062401.
- [59] N. Schulz, G. Pantano, D. DeTelle, A. Chanda, E. M. Clements, M. McGuire, A. Markou, C. Felser, D. A. Arena, J. Gayles, M. H. Phan, H. Srikanth, *Phys. Rev. B* **2024**, *110*, 054419.
- [60] Z. H. Liu, M. Zhang, Y. T. Cui, Y. Q. Zhou, W. H. Wang, G. H. Wu, X. X. Zhang, G. Xiao, *Appl. Phys. Lett.* **2003**, *82*, 424.
- [61] M. Acet, Ll. Mañosa, A. Planes, *Handb. Magn. Mater.* **2011**, *19*, 231.
- [62] A. Banerjee, P. Chaddah, S. Dash, K. Kumar, A. Lakhani, X. Chen, R. V. Ramanujan, *Phys. Rev. B* **2011**, *84*, 214420.
- [63] R. Y. Umetsu, K. Kobayashi, A. Fujita, R. Kainuma, K. Ishida, K. Fukamichi, A. Sakuma, *Phys. Rev. B* **2008**, *77*, 104422.
- [64] M. Sargolzaei, M. Richter, K. Koepf, I. Opahle, H. Eschrig, I. Chaplygin, *Phys. Rev. B* **2006**, *74*, 224410.
- [65] Z. Zhu, T. Higo, S. Nakatsuji, Y. Otani, *AIP Adv.* **2020**, *10*, 085020.
- [66] K. Manna, L. Muechler, T.-H. Kao, R. Stinshoff, Y. Zhang, J. Gooth, N. Kumar, G. Kreiner, K. Koepf, R. Car, J. Kübler, G. H. Fecher, C. Shekhar, Y. Sun, C. Felser, *Phys. Rev. X* **2018**, *8*, 041045.
- [67] D. Miura, A. Sakuma, *J. Phys. Soc. Jpn.* **2022**, *91*, 023706.
- [68] X. Wu, Z. Liu, *J. Appl. Phys.* **2018**, *123*, 085109.
- [69] W. B. Yelon, L. Berger, *Phys. Rev. B* **1972**, *6*, 1974.
- [70] Y. Hsu, L. Berger, *Phys. Rev. B* **1976**, *14*, 4059.

- [71] C. Guillemard, S. Petit-Watelot, J.-C. Rojas-Sanchez, J. Hohlfeld, J. Ghanbaja, A. Bataille, P. Le Fèvre, F. Bertran, S. Andrieu, *Appl. Phys. Lett.* **2019**, *115*, 172401.
- [72] M. R. Natale, D. J. Wesenberg, E. R. J. Edwards, H. T. Nembach, J. M. Shaw, B. L. Zink, *Phys. Rev. Mater.* **2021**, *5*, L111401.
- [73] J. Sootsman, D. Chung, M. Kanatzidis, *Angew. Chem., Int. Ed.* **2009**, *48*, 8616.
- [74] T. Tadano, Y. Gohda, S. Tsuneyuki, *J. Phys.: Condens. Matter* **2014**, *26*, 225402.
- [75] T. Tadano, S. Tsuneyuki, *J. Phys. Soc. Jpn.* **2018**, *87*, 031015.
- [76] G. Kresse, J. Furthmüller, *Phys. Rev. B* **1996**, *54*, 11169.
- [77] G. Kresse, D. Joubert, *Phys. Rev. B* **1999**, *58*, 1758.
- [78] J. P. Perdew, K. Burke, M. Ernzerhof, *Phys. Rev. Lett.* **1996**, *77*, 3865.